

MECHANISM OF ATOMIC HYDROGEN ADDITION REACTIONS ON NP-ASW

JIAO HE¹ AND SHAHNEWAJ M. EMTIAZ AND GIANFRANCO VIDALI²

Physics Department, Syracuse University, Syracuse, NY 13244, USA

¹jhe08@syr.edu

²gvidali@syr.edu

ABSTRACT

Hydrogen, being the most abundant element, is the driver of many if not most reactions occurring on interstellar dust grains. In hydrogen atom addition reactions, the rate is usually determined by the surface kinetics of the hydrogen atom instead of the other reaction partner. Three mechanisms exist to explain hydrogen addition reactions on surfaces: Langmuir-Hinshelwood, Eley-Rideal, and hot-atom. In gas-grain models, which mechanism is assumed greatly affects the simulation results. In this work, we quantify the temperature dependence of the rates of atomic hydrogen addition reactions by studying the reaction of $\text{H} + \text{O}_3 \rightarrow \text{O}_2 + \text{OH}$ on the surface of a film of non-porous amorphous solid water (np-ASW) in the temperature range from 10 K to 50 K. The reaction rate is found to be temperature independent. This disagrees with the results of simulations with a network of rate equations that assume Langmuir-Hinshelwood mechanism through either thermal diffusion or tunneling diffusion; the reaction rates assuming such mechanism possesses a strong temperature dependence, either explicitly or implicitly, that is not seen experimentally. We suggest that the Eley-Rideal and/or hot-atom mechanism play a key role in hydrogen atom addition reactions, and should be included in gas-grain models. We also suggest that our newly developed time-resolved reactive scattering can be utilized to measure the chemical desorption efficiency in grain surface reactions.

Keywords: ISM: molecules — ISM: atoms — methods: laboratory: solid state — methods: laboratory: atomic — Physical Data and Processes: astrochemistry

1. INTRODUCTION

In the last decade, it has become increasingly evident that molecules that are key to physical and chemical processes in the interstellar medium, such as H_2 , H_2O , H_2CO , CH_3OH and many others, are formed exclusively or in large part on and in ices coating dust grains (Herbst & van Dishoeck 2009; Garrod & Widicus Weaver 2013). Evidence has come from observations (Tielens 2013), laboratory experiments (Vidali 2013), and simulations (Garrod et al. 2008). In quiescent dense clouds, where there is little UV flux, it can be argued that many of the reactions are due to neutral atoms and radicals from the gas-phase impinging on ice-coated dust grains and reacting with atoms and molecules on them (Linnartz et al. 2015). How these reactions occur and at what rates is of paramount importance in order to characterize and assess the role that dust grains play in the chemical evolution of the ISM. One of the central questions is the role of diffusion of the hydrogen atom that has landed on the surface of a grain (Biham et al. 2001; Cuppen & Herbst 2005; Cazaux et al. 2005; Hama et al. 2012; Iqbal et al.

2012). As an H atom approaches the surface of a dust grain, the H atom can react with an atom or molecule on the surface through a direct hit (Eley-Rideal mechanism), or it can make a few hops moving at super thermal speed and then react (hot-atom mechanism). In both cases, there is little or no energy accommodation with the surface. The third way of making a molecule is the familiar Langmuir-Hinshelwood mechanism where the incoming hydrogen atom becomes thermally accommodated with the surface. Hydrogen atoms move on the surface either via thermal hopping, which obeys an Arrhenius type expression, or via quantum tunneling, which is independent of surface temperature. A gas-grain model assuming different mechanisms would yield dramatically different results. Therefore, to characterize how reactions occur on surfaces and obtain realistic prediction of the grain surface chemistry, one needs to assess the mobility of hydrogen and reaction mechanisms. This type of information is of great importance for simulations of the chemical evolution of ISM environments, and is currently largely unavailable for systems of interest to astrophysics. In this work, we focused our attention on

measuring the cross-section of the $\text{H}+\text{O}_3 \rightarrow \text{O}_2+\text{OH}$ reaction, where O_3 resides on the surface of water ice, and deriving the mobility of atomic hydrogen on the surface of water ice based on the cross-section (Takahashi et al. 1999).

In some reactions, the resulting molecule keeps a good fraction of the gained bond energy and is ejected with high translational and ro-vibrational energy (Creighan et al. 2006; Gavilan et al. 2014). Sometimes the ejection of the molecule due to this type of non-thermal desorption caused by the reaction is called chemical desorption (Takahashi & Williams 2000) to distinguish it from thermal desorption that occurs when a particle leaves a surface because of its thermal energy. These mechanisms have been verified and characterized in interaction of $\text{H}(\text{D})$ with $\text{D}(\text{H})$ loaded single crystal surfaces, mostly metals (e.g. Jackson et al. 2002). Few experiments showing these two mechanisms have been carried out for astrophysical relevant systems, mostly on graphitic (Creighan et al. 2006; Gavilan et al. 2014) and polycyclic aromatic hydrocarbons (PAHs) surfaces (Mennella et al. 2012). Chemical desorption of H_2O due to the reaction of oxygen and hydrogen on silicate was detected by Dulieu et al. (2013). Minissale et al. (2016) reported an extensive list of chemical desorption efficiencies of various grain surface reactions; however, no detailed supporting experimental data were provided. In this study we use a newly developed method — time-resolved reactive scattering — to measure directly the chemical desorption efficiency of $\text{H}+\text{O}_3 \rightarrow \text{O}_2+\text{OH}$ and demonstrate how to utilize this technique to measure the chemical desorption efficiency. We then carry out simulations to show that the Eley-Rideal/hot-atom mechanism has to be incorporated in simulations of atom addition reactions on grain surfaces.

The paper is structured as follows. The apparatus is described in the next Section. In Section 3 the experimental methods, results and their analysis are presented. The significance of these measurements for characterizing chemical reactions on surfaces is given in Section 4.

2. APPARATUS

Experiments were performed in a ultra-high vacuum (UHV) chamber (He et al. 2015, 2016a). At the center of the 10 inch diameter stainless steel chamber there is a 1 cm^2 gold coated copper disk that can be cooled down to 8 K using liquid helium or heated up to 450 K using a cartridge heater. The temperature of the sample disk is measured and controlled by a Lakeshore 336 temperature controller with an accuracy better than 0.05 K. A Hiden Analytical quadrupole mass spectrometer (QMS) mounted on a rotatable platform can directly face one of the molecular beams to measure beam

composition, or face the sample to measure molecules coming off the sample. A gas capillary array is placed behind the sample holder to deposit water vapor into the chamber for ice growth. In this study, experiments were performed either on a clean gold surface or non-porous amorphous solid water (np-ASW). The growth of water ice has been described in He et al. (2016a); here we briefly summarize it. The np-ASW sample was grown by background deposition of water vapor onto the gold substrate when the substrate was at 130 K. The water vapor pressure during deposition was 5×10^{-7} torr, and the deposition duration was 200 s, amounting to about 100 Langmuir of water ice. After water deposition, the ice sample was annealed at 130 K for 30 minutes, during which the pressure in the chamber drops to middle 10^{-10} torr range. Water ice prepared this way is np-ASW (Stevenson et al. 1999). Connected to the main reaction chamber are two three-stage differentially pumped atomic/molecular beamlines. In this study only one beam was used. The first stage of the beamline houses a radio-frequency (RF) powered dissociation source with an inductive coil wrapped around a water cooled Pyrex glass tube. The end of the source was capped by an aluminum nozzle with an inner diameter of 1 mm. Under the feeding pressure we used, the beam was effusive with a Boltzmann velocity distribution characterized by a temperature of ~ 300 K. An Alicat MCS-5 mass flow controller was used to accurately control the gas flow to the dissociation source. Gas specific correction factors are already taken into account by the flow controller. The beam flux was calibrated using temperature programmed desorption (TPD) experiments (He et al. 2016a). For experiments performed in this study, the H_2 and O_2 flow were 1.4×10^{-2} ML/s and 5.6×10^{-3} ML/s, respectively. The uncertainty in flow rate is mostly due to the uncertainty in determining the monolayer coverage in the TPD experiments, and it is estimated to be about 30%. When the RF power was turned on, the dissociation rates for H_2 and O_2 were about 70% and 30%, respectively. Based on a previous measurement of the speed of the atomic beam, atoms from the source are well thermalized with the Pyrex glass wall (He et al. 2016b). The second stage of the beamline houses an in-vacuo DC motor driving a chopper disk with a single open slit with a 1/40 duty factor. For experiments performed in this study, the chopper spinning speed was set to 50 ± 1 Hz. A pair of LED and photodiode located at the opposite sides of the chopper disk was used to monitor the opening and closing of the beam. The pulse signal generated by the photodiode when the 1/40 open slit was lined up with the LED-photodiode pair was fed into a multichannel scaler (MCS) coupled with the QMS. This provide capability to measure the in-phase intensity of the beam or the

molecules desorbing from the surface. During a typical in-phase measurement in this work, the dwell time of the MCS, which is also the time resolution of the time-of-flight spectra, was set to 20 μ s, and a total of 10,000 or 20,000 scans were averaged to increase the signal-to-noise ratio. Considering the period of the chopper disk, 20 ms, and the duty cycle, 1/40, the equivalent H exposure time, 5 to 10 seconds, results in a small dose to the sample. The consumption of ozone by H was only a small fraction of a monolayer. For simplicity, in later discussions we assume that the ozone coverage was always 1 ML during the in-phase measurements. More details of the in-phase detection can be found in He et al. (2016b). In the third stage of the beamline, a stepper motor controlled flag automates the opening and closing of the beam. A LabVIEW program controls the stepper motor so that the uncertainty in the beam open time is less than 50 ms.

3. EXPERIMENTS, RESULTS AND ANALYSIS

3.1. Preparation of the ozone layer

The ozone layer was prepared following a procedure as described in He & Vidali (2014b). With the substrate at 20 K, the dissociated oxygen beam was sent onto the sample. The atomic oxygen and undissociated molecular oxygen react and form ozone. The sample was then brought up to 50 K and annealed at 50 K for a few minutes to remove molecular oxygen, leaving ozone on the surface. In certain conditions, a small fraction (less than $\sim 1\%$) of atomic oxygen may still be present (He et al. 2015). We will ignore the effect of atomic oxygen because it is small compared to other uncertainties. The ozone was then cooled down to a lower temperature for further experiments. A complete set of ozone TPD experiments with different O/O₂ deposition durations were performed on a gold surface. The TPD traces are shown in Figure 1. At low coverages, ozone molecules tend to occupy deep adsorption sites and desorb at relatively high temperatures. As the coverage increases from 0.2 ML to 1.0 ML, deeper sites are filled gradually and ozone molecules occupy shallower sites with lower desorption temperatures. The decrease in desorption peak temperature is accompanied by a decrease in the gap between the leading edges of successive traces decreases. Above 1 ML, the desorption is zeroth order with the typical overlapping leading edges. We determine the one monolayer coverage based on the gap of the leading edges. This method of thickness calibration is the same as the one used in several other works (He & Vidali 2014a; Smith et al. 2016; He et al. 2016a). The calibration of TPD experiments of different molecules such as O₂ and CH₄ (not shown here) demonstrated that the number of adsorption sites per unit area

of np-ASW is similar to that of gold coated copper disk used as sample. This suggests that it takes the same amount of O/O₂ exposure to cover np-ASW with one ML of O₃ as to cover the gold surface. Therefore the calibration of ozone coverage on the gold surface applies to the np-ASW surface.

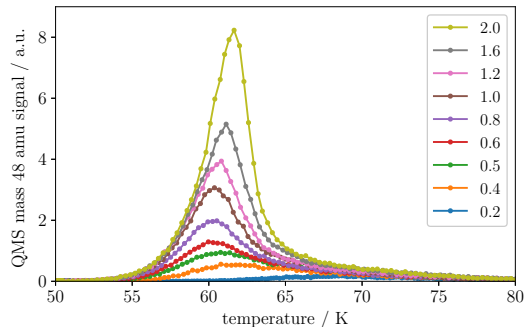


Figure 1. Temperature programmed desorption (TPD) traces of ozone on a gold surface. Heating ramp rate during TPD was 0.5 K/s. Surface coverage is shown in the inset in the unit of monolayer (ML).

3.2. Time-resolved reactive scattering in H+O₃ experiments

In the H+O₃ \rightarrow O₂+OH reaction, depending on the surface temperature, a fraction of the reaction product O₂ leaves the surface via either thermal desorption or chemical desorption. The thermal desorption has the well-known rate given by the Arrhenius-type expression $\nu \exp(-E_{\text{des}}/k_{\text{B}}T)$, where ν is the desorption pre-factor, E_{des} is the desorption energy (or binding energy), k_{B} is the Boltzmann constant, and T is the surface temperature. Thermal desorption has a strong dependence on the temperature. Chemical desorption occurs when the heat released in the reaction makes the product (O₂ in this case) leave the surface. Usually the chemical desorption rate is insensitive to the surface temperature because the energy from the reaction is much higher than the binding energy, especially for weakly bounded species like O₂. Therefore, by studying the reaction at different surface temperature we should be able to distinguish the two mechanisms of desorption. At relative high surface temperature ($T > 35$ K) the thermal desorption rate of O₂ is high, and all O₂ leave the surface within a short time, whether thermally or chemically. In H+O₃ experiments carried out at low surface temperatures ($T < 25$ K), the thermal desorption rate is negligible but the chemical desorption rate should remain the same as that of high temperature. The chemical desorption efficiency, which is defined as the fraction of reaction products that leave the surface due to the exothermicity of the reaction, can be approximately calculated as

the desorption yield at low temperature divided by the desorption yield at high temperature.

To determine the desorption rate of O_2 accurately, we used an in-phase detection, the time-resolved reactive scattering (TRRS) method, because the traditional method of using the QMS is inadequate for the measurement of the chemical desorption rate. Typically a QMS has a time scale (dwell time) of a few hundred milliseconds, so it is not possible to separate chemically desorbed molecules from those thermally desorbed with a residence time comparable with the QMS time scale. To overcome this difficulty of conventional QMS measurement, we used a modulated atomic hydrogen beam and multichannel scaler (MCS) coupled with the QMS to measure the in-phase signal of O_2 , so that the O_2 that leaves the surface due to chemical desorption can be separated from the thermally desorbed O_2 . The in-phase detection also increase the sensitivity of the measurements because the O_2 contribution from the chamber background is subtracted out. In addition, the sample holder, which is also at low temperature, may act as a cryopump with a changing pumping speed. This affects the O_2 measured by the QMS. In-phase detection overcomes these problems. A more detailed description of the advantage of in-phase detection can be found in [He et al. \(2016b\)](#).

To obtain the temperature dependence of reaction cross-section of $H+O_3 \rightarrow O_2+OH$, atomic hydrogen was deposited on top of a full layer of ozone at 10, 20, 30, 40, and 50 K. In the in-phase measurements, to ensure that $H+O_3$ experiments done at different temperatures start from the same initial condition, the initial surface for each experiment was fully covered with one monolayer of ozone, and the subsequent H exposure was kept short. Based on prior discussion, the change in ozone coverage during H exposure is a small fraction of one monolayer. Therefore an incoming H atom always sees a whole layer of ozone, and the underlying substrate does not play a role in the reaction. The resulting time-resolved reactive scattering of O_2 from $H+O_3$ is shown in Figure 2. The x-axis shows the time delay respect to the time when the chopper slit is aligned up with the beam, and the y-axis shows the averaged mass 32 amu pulse counts within $20 \mu\text{m}$ bins. The spread of the peak in Figure 2 is mostly due to the time of flight from the chopper to the sample. The distance from the chopper to the sample is much longer than the distance from the sample to the QMS detector. In our previous paper ([He et al. 2016b](#)), we reported that the spread of the peak is consistent with an effusive beam at room temperature with Maxwell-Boltzmann distribution. The measured mass 32 amu signal can also be due to other reaction products, such as HO_2 and H_2O_2 . For now, we assume that the mass 32 amu signal is solely due to O_2 . Later, we'll show that

other contributions to mass 32 amu signal only amount to a small fraction of the O_2 signal. At 50 K, the O_2 desorption is the highest. From 50 to 30 K, the desorption of O_2 drops dramatically because of the change in the thermal desorption rate. At 30, 20, and 10 K, the mass 32 amu desorption rates are almost the same, indicating that the thermal desorption rate is zero and the desorption is exclusively chemical. The inset shows the mass 32 amu desorption rate at 10 K is 0.11 times as the desorption rate at 50 K. Therefore the chemical desorption rate is 11% of the total desorption rate of O_2 . We only carried out the $H+O_3$ measurement at up to 50 K, because at higher surface temperatures ozone starts to desorb during the experiment. We do not exclude the possibility that at 50 K, there is thermal desorption of a small fraction of O_2 with a residence time longer than the time scale of MCS measurement (a few ms). These molecules would show up as background and be subtracted out, therefore an underestimation of the total O_2 desorption is possible. We conclude that the chemical desorption rate of O_2 produced by $H+O_3$ could be slightly less than 11% of the total desorption rate. This value is close to the measurement by [Minissale et al. \(2016\)](#) which found the upper limit to be 10% and 8% on amorphous silicate and oxidized HOPG, respectively.

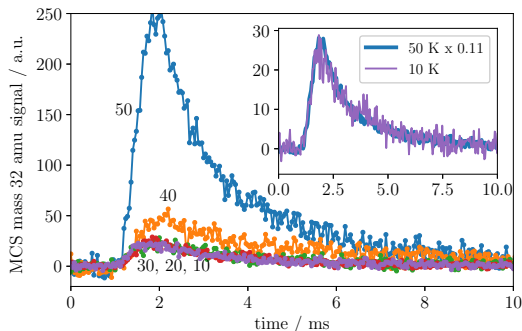


Figure 2. Multichannel scaler signal of mass 32 amu during the exposure of pulses of atomic hydrogen beam on 1 ML of ozone on np-ASW. The signal is averaged over 10000 or 20000 cycles. The surface temperature is shown in the figure. The inset shows a comparison between the trace at 50 K and that at 10 K.

3.3. Measurement of the $H+O_3$ cross section

In order to measure the reaction cross-section of $H+O_3$, we carried out another set of experiments without in-phase detection. We irradiated the ozone sample at 50, 40, 30, 20, and 10 K with H for an extended period of time until the ozone was used up. In each of these measurements, 1 ML of ozone was prepared on the np-ASW surface before atomic hydrogen deposition. The ozone sample was irradiated until the desorption of O_2 became negligible. The QMS was used to monitor the

decay of O_2 , see Figure 3. At the very beginning of H exposure, the surface is fully covered with O_3 and the reaction rate does not drop with time. It also suggests that the initial ozone coverage might be slightly more than 1 ML. When the ozone coverage becomes less than 1 ML the reaction rate decays exponentially. The traces for different temperatures, plotted in a semi-log scale, are fitted well with straight lines. We confirmed that the measured mass 32 amu signal is due to the reaction $H+O_3$ instead of air contamination in the H/H_2 beam by aligning the QMS detector entrance with the beam and measuring the beam composition directly.

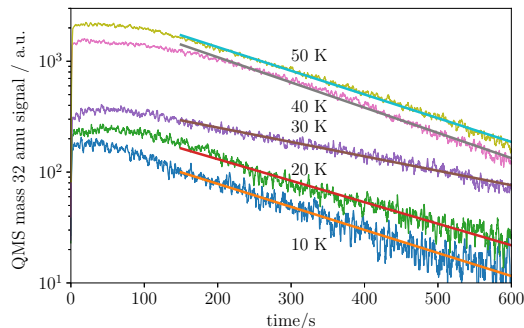


Figure 3. The mass 32 amu signal measured by the QMS during atomic hydrogen exposure on 1 ML of ozone at 10, 20, 30, 40, and 50 K. The hydrogen atom beam flux is about 2×10^{-2} ML/s. The straight lines are fits using an exponential decay law, see text.

The following reactions are likely to occur on the surface:



At 50 K and 40 K, almost all of the O_2 that is formed leaves the surface within a very short time. O_2 does not build up on the surface. Reactions R1 and R2 dominate. At 10 K and 20 K, most of O_2 remains on the surface and can react with atomic hydrogen via R3. Almost all of the above reactions are involved. In Figure 3, notice that the desorption at 40 K is lower than that of 50 K. This difference is likely due to the fact that the effective pumping speed of the sample holder is higher when the sample is at 40 K than at 50 K (He et al. 2016b). At lower temperatures the traces are much lower, both because of the difference in pumping speed and a lower

thermal desorption rate of mass 32 amu at lower temperatures. The exponential decay in O_2 is similar at all temperatures except at 30 K. The anomalous behavior at 30 K can be explained by the coverage dependence of O_2 binding energy. At 50 and 40 K, no O_2 builds up on the surface, and the thermal desorption rate is not changing with time. At 30 K, at the beginning of the H exposure, the O_2 coverage is low and the binding energy is high, and the thermal desorption rate is low. As O_2 builds up, O_2 has to occupy sites with progressively weaker binding energy and therefore the thermal desorption of O_2 increases. More details on the coverage dependence of binding energy can be found in He et al. (2016a). Therefore, there is significant change in slope of the O_2 decay at 30 K with respect to at 40 and 50 K. At 20 K and 10 K, O_2 does not thermally desorb and stays on the surface except for those O_2 that chemically desorb. O_2 reacts with atomic hydrogen, leading to the products, HO_2 and H_2O_2 ; they could all be possible sources of mass 32 amu in the QMS as shown in Figure 3, because they can be ionized to O_2^+ in the QMS. To calculate the reaction cross-section of $H+O_3$, the contribution from the other two molecules has to be subtracted. This is discussed next.

To find out how reactions R3 and R4 contribute to the mass 32 amu signal in the QMS, we studied $H+O_2$ and $H+O_3$ reactions under the same conditions. An np-ASW surface was covered with 1.7 ML of O_2 or 1 ML of O_3 , and then exposed to the H beam until the O_2/O_3 was consumed and mass 32 amu signal dropped to the background level. The measurements were carried out both at 10 K and 20 K. The mass 32 amu signal was recorded during the H exposure, as shown in Figure 4. We excluded the possibility that H_2 (which is present as the undissociated fraction in the beam) sputters off O_2 ice by sending an H_2 beam onto O_2 ice. No O_2 sputtered off the sample was detected. The only possibility left to explain the mass 32 signal during H exposure to O_2 is that HO_2 desorbs and is detected in the QMS as mass 32 amu (O_2^+). HO_2 most likely (partly) chemically desorbs from the surface and is efficiently broken up in the QMS ionizer. From the comparison between $H+O_2$ and $H+O_3$, one can see that in the same condition, $H+O_2$ only introduces $\sim 20\%$ of mass 32 amu as that of $H+O_3$. If we take the chemical desorption efficiency of reaction R1 as 0.11, then the chemical desorption efficiency for reaction R3 is $0.2 \times 0.11 = 0.022$. It should be noted that we are assuming the detection efficiency of HO_2 (as mass 32 amu) and O_2 are the same in the QMS. But even without this assumption, a similar conclusion for the $H+O_3$ reaction cross-section can be reached, because the chemical desorption rate of R3 is trivial. It should be also noted that in $H+O_3$ the mass 32 amu signal increases as soon as the H exposure begins, while

in $\text{H}+\text{O}_2$ the mass 32 amu signal does not jump to maximum right away. This delay may be attributed to a small reaction energy barrier in reaction R3. Quantifying the barrier of reaction R3 is out of scope of this work and we assume it is barrierless hereafter. In both $\text{H}+\text{O}_2$ and $\text{H}+\text{O}_3$ experiments, we also checked other masses, and no significant changes in mass 17, 18, 33, and 34 amu signals were seen during H exposure. Based on our previous measurements, if H_2O_2 desorbs, mass 34 amu should be seen from the QMS signal. Non-detection of mass 34 during H exposure suggests that H_2O_2 does not contribute significantly to the mass 32 amu signal. The mass 32 amu signal is mostly due to the desorption of O_2 , and a small contribution from HO_2 most likely because it partly chemically desorbs from the surface and is efficiently broken up in the QMS ionizer.

3.4. Rate equation simulations

We used a simple set of rate equations to describe the interaction of H with O_3 . For atomic hydrogen addition reactions, we consider all three possibilities: Langmuir-Hinshelwood, quantum tunneling, and Eley-Rideal/hot-atom mechanisms. To avoid complications, we only consider one mechanism at a time to see the effect of each of them. Based on Reactions R1 to R6, we come up with the following rate equations to describe the reaction network:

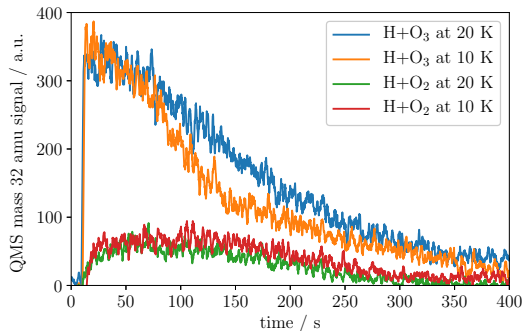


Figure 4. Mass 32 amu signal during H exposure on 1.7 ML of O_2 (bottom two traces) and 1 ML of ozone (top two traces) at 10 K and 20 K. The measurements were performed on an np-ASW sample.

$$\Psi = \begin{cases} \phi\sigma_{\text{ER}}, & \text{E-R or H-A} \\ \nu N(\text{H}) \exp(-\frac{E_{\text{diff,H}}}{k_{\text{B}}T}), & \text{L-H} \\ \nu N(\text{H}) \exp(-2a\sqrt{2m_{\text{H}}E_{\text{diff,H}}}/\hbar), & \text{tunneling} \end{cases} \quad (1)$$

$$\frac{dN(\text{O}_3)}{dt} = -\Psi N(\text{O}_3) \quad (2)$$

$$\frac{dN(\text{O}_2)}{dt} = (1 - R_1)\Psi N(\text{O}_3) - \nu N(\text{O}_2) \exp(-\frac{E_{\text{des,O}_2}}{k_{\text{B}}T}) - \Psi N(\text{O}_2) \quad (3)$$

$$\frac{dN(\text{HO}_2)}{dt} = (1 - R_2)\Psi N(\text{O}_2) - \Psi N(\text{HO}_2) \quad (4)$$

$$\frac{dN(\text{H}_2\text{O}_2)}{dt} = \Psi N(\text{HO}_2) - \Psi \exp(-\frac{E_{\text{a}}}{k_{\text{B}}T})N(\text{H}_2\text{O}_2) \quad (5)$$

$$\frac{dN(\text{H}_2\text{O})}{dt} = \Psi N(\text{OH}) + \Psi \exp(-\frac{E_{\text{a}}}{k_{\text{B}}T})N(\text{H}_2\text{O}_2) \quad (6)$$

$$\frac{dN(\text{OH})}{dt} = \Psi N(\text{O}_3) + \Psi \exp(-\frac{E_{\text{H}_2\text{O}_2}}{k_{\text{B}}T})N(\text{H}_2\text{O}_2) - \Psi N(\text{OH}) \quad (7)$$

$$\begin{aligned} \frac{dN(\text{H})}{dt} = & \phi - \nu N(\text{H}) \exp(-\frac{E_{\text{des,H}}}{k_{\text{B}}T}) - \Psi N(\text{H}_2\text{O}_2) \exp(-\frac{E_{\text{a}}}{k_{\text{B}}T}) - \\ & \Psi(2N(\text{H}) + N(\text{O}_3) + N(\text{O}_2) + N(\text{HO}_2) + N(\text{OH})) \end{aligned} \quad (8)$$

N_{xx} are the coverage of different species on the surface, and they have the dimensionless-unit of ML. Ψ is the term linked to the rate of atomic hydrogen addition reactions. ϕ is the incoming atomic hydrogen flux. σ_{ER} is the reaction cross-section in the E-R or H-A mechanism. Since both the E-R and the H-A mechanisms follow similar numerical expressions, except that they have different values of the reaction cross-section, we treat them indifferently in the rate equation simulations. The chemical desorption efficiency of reactions **R1** and **R3** are represented by R_1 and R_2 , respectively. The chemical desorption of OH from H+O₃ was checked by measurement, and no significant OH desorption was seen using the QMS. In Reaction **R5**, the reaction energy barrier E_{a} is taken to be 2100 K (Koussa et al. 2006). All other reactions are taken to be barrierless (Cuppen et al. 2010; Mokrane et al. 2009). The thermal desorption of O₂ is calculated by assuming a single value, 1200K, of the binding energy, although ideally a continuous distribution should be used instead (He et al. 2016a). The binding energy of H on AWS is taken to be 450 K (Garrod & Herbst 2006). Different values of $\alpha = E_{\text{diff}}/E_{\text{des}}$ ratio were tried in the simulation. But only simulation results with $\alpha = 0.7$ are presented as an illustration. The desorption of HO₂, H₂O, and H₂O₂ are ignored in the simulation because there is negligible desorption of these molecules during the H exposure.

Before presenting the simulation results, we do a qualitative analysis of the reaction cross-section. Based on Figure 3, the exponential decay rate of mass 32 amu signal is similar at 10, 20, 40, and 50 K. Little tem-

perature dependence is seen. Therefore the value of Ψ should have little temperature dependence between 10 K and 50 K. In the expression for L-H mechanism, a strong temperature dependence is expected because of the Arrhenius type expression. In the expression of diffusion by tunneling there is no explicit temperature dependence; however, the coverage of hydrogen atoms on the surface $N(\text{H})$ strongly depends on the surface temperature. Therefore the only mechanisms that do not possess temperature dependence are the E-R and H-A mechanisms. Yuan et al. (2014) explained temperature independent reaction rate of OH+CO→CO₂+H by E-R mechanism in a similar way.

In the simulations assuming the L-H mechanism, different values of the H binding energy and diffusion energy barrier were tried, but none were able to yield exponential decay curves with little temperature dependence, as observed experimentally. The results of one of the simulations are shown in Figure 6. The L-H mechanism is unable to explain the measured data in Figure 3. Similarly, we also confirmed that quantum tunneling diffusion mechanism is unable to produce temperature independent exponential decay curves as in Figure 3. The Eley-Rideal/hot-atom mechanism has to be used instead. The cross-section in the E-R/H-A mechanism that best reproduces the traces in Figure 3 is shown in Table 1. The cross-section is calculated in the unit of the number of square lattices. The third column is calculated using an adsorption sites density of 1.5×10^{15} cm⁻², although different densities have been assumed in previous models. The relative errors of the values of

the cross-section are mostly due to the uncertainty in fitting and the fluctuation of the atomic hydrogen flux, and they are estimated to be less than 5%. However, the absolute error, which is mostly due to the uncertainty in determining the surface coverage, can be as large as 30%. The cross-sections at different temperatures are close with little temperature dependence; and they are smaller than the area of a square lattice, indicating that H does not move much on the surface.

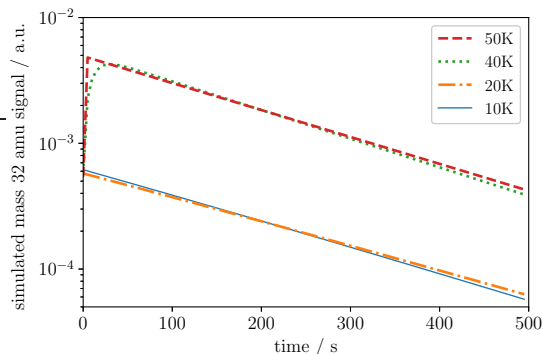


Figure 5. Simulated mass 32 amu signal using the rate equations model, assuming the Eley-Rideal/hot-atom mechanism. The parameters used in the simulation are shown in Table 2.

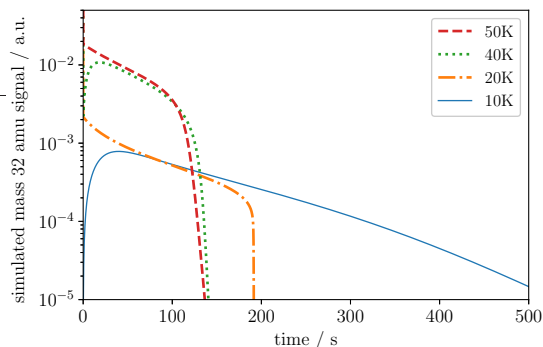


Figure 6. As in Figure 5, but assuming the Langmuir-Hinshelwood mechanism.

4. ASTROPHYSICAL IMPLICATIONS

Reactions on surfaces of dust grain analogs involving hydrogen atoms are the dominant reactions that govern grain surface chemistry. How hydrogen atoms take part in the reactions, and specifically what is the mechanism for the diffusion of hydrogen atoms, are important issues in astrophysics. Here, in this work we demonstrated that the reaction between hydrogen atoms and ozone — a venue to form water on surfaces (Tielens & Hagen 1982) — cannot be explained by using the Langmuir-Hinshelwood mechanism, either with thermal diffusion or quantum tunneling diffusion. Eley-Rideal or hot-atom type mechanisms have to be involved to interpret

Table 1. Cross-section of the reaction $\text{H}+\text{O}_3 \rightarrow \text{O}_2+\text{OH}$ on np-ASW at different temperatures calculated using a rate equation model assuming Eley-Rideal/hot-atom mechanism for atomic hydrogen. The second column is the cross-section in the unit of l_0^2 , where l_0 is the distance between two nearest adsorption sites. The cross-section in the third column is calculated assuming an adsorption site density of $1.5 \times 10^{15} \text{ cm}^{-2}$.

temperature	cross-section/ l_0^2	cross-section/ \AA^2
10	0.28	1.89
20	0.27	1.77
40	0.27	1.77
50	0.25	1.66

Table 2. Parameters in the rate equation simulation for results in Figure 5 and Figure 6.

Parameter	Value
$E_{\text{des,H}}$	450 K
$E_{\text{des,O}_2}$	1200 K
$E_{\text{diff,H}}$	315 K
E_a	2100 K
ν	10^{12} s^{-1}
ϕ	$0.020 \text{ ML}\cdot\text{s}^{-1}$
R_1	0.11
R_2	0.022

the experimental data. Although in our experiment we started with a full layer of ozone on np-ASW, the conclusion that the reaction is E-R is based on the analysis of the $\text{H}+\text{O}_3$ reaction over the entire coverage range of ozone. Our conclusions regarding the mechanisms of reactions involving hydrogen atoms can be generalized to other barrierless and low-barrier hydrogen atom addition reactions on grain surfaces, because the reaction rate is governed by the kinetics of hydrogen atoms instead of the one of ozone or other reactants. We studied the reaction with H atoms at thermal energy ($\sim 300\text{K}$), while H atoms in certain environments — such as in dense clouds — may have lower kinetic energies, and it is possible that the cross-section values have to be modified. But the mechanism of the reaction should still be the same. In the case that the reaction has a barrier, the rate needs to be multiplied by $\exp(-E/k_{\text{B}}T)$, where E is the reaction energy barrier. In most existing gas-grain models, the Langmuir-Hinshelwood mechanism is the main mechanism considered, if not the only mechanism, although there are now models incorporating Eley-Rideal or hot-atom mechanisms to study the formation of molecules in the ISM (Ruaud et al. 2015). For hydrogen atoms, quantum tunneling diffusion needs

also to be considered, although it depends greatly on the morphology of the surface. The main result of our work is that our laboratory measurements and simulations demonstrate the importance of Eley-Rideal and/or hot-atom mechanisms. Together with the other mechanisms, they have to be incorporated in models of surface reactions with hydrogen atoms.

5. ACKNOWLEDGMENTS

We would like to thank Eric Herbst and Ilsa Cooke for their helpful suggestions and Xixin Liang for technical assistance. We are grateful to an anonymous referee for the constructive comments that helped to improve the paper. This work was supported by NSF Astronomy & Astrophysics Research Grants No.1311958 and No.1615897.

REFERENCES

- Biham, O., Furman, I., Pirronello, V., & Vidali, G. 2001, *ApJ*, 553, 595
- Cazaux, S. M., Caselli, P., Walmsley, M., & Tielens, A. G. G. M. 2005, in *IAU Symposium*, Vol. 231, *Astrochemistry: Recent Successes and Current Challenges*, ed. D. C. Lis, G. A. Blake, & E. Herbst, 325–336
- Creighan, S. C., Perry, J. S. A., & Price, S. D. 2006, *JChPh*, 124, 114701
- Cuppen, H. M., & Herbst, E. 2005, *MNRAS*, 361, 565
- Cuppen, H. M., Ioppolo, S., Romanzin, C., & Linnartz, H. 2010, *Physical Chemistry Chemical Physics (Incorporating Faraday Transactions)*, 12, 12077
- Dulieu, F., Congiu, E., Noble, J., et al. 2013, *Scientific Reports*, 3, 1338
- Garrod, R. T., & Herbst, E. 2006, *A&A*, 457, 927
- Garrod, R. T., Weaver, S. L. W., & Herbst, E. 2008, *ApJ*, 682, 283
- Garrod, R. T., & Widicus Weaver, S. L. 2013, *Chemical Reviews*, 113, 8939
- Gavilan, L., Lemaire, J. L., Vidali, G., Sabri, T., & Jæger, C. 2014, *ApJ*, 781, 79
- Hama, T., Kuwahata, K., Watanabe, N., et al. 2012, *ApJ*, 757, 185
- He, J., Acharyya, K., & Vidali, G. 2016a, *ApJ*, 825, 89
- , 2016b, *ApJ*, 823, 56
- He, J., Shi, J., Hopkins, T., Vidali, G., & Kaufman, M. J. 2015, *ApJ*, 801, 120
- He, J., & Vidali, G. 2014a, *Faraday Discussions*, 168, 517
- , 2014b, *ApJ*, 788, 50
- Herbst, E., & van Dishoeck, E. F. 2009, *ARA&A*, 47, 427
- Iqbal, W., Acharyya, K., & Herbst, E. 2012, *ApJ*, 751, 58
- Jackson, B., Sha, X., & Guvenc, Z. B. 2002, *JChPh*, 116, 2599
- Koussa, H., Bahri, M., Jadane, N., & Lakhdar, Z. B. 2006, *Journal of Molecular Structure: THEOCHEM*, 770, 149
- Linnartz, H., Ioppolo, S., & Fedoseev, G. 2015, *International Reviews in Physical Chemistry*, 34, 205
- Mennella, V., Hornekær, L., Thrower, J., & Accolla, M. 2012, *ApJL*, 745, L2
- Minissale, M., Dulieu, F., Cazaux, S., & Hocuk, S. 2016, *A&A*, 585, A24
- Mokrane, H., Chaabouni, H., Accolla, M., et al. 2009, *ApJL*, 705, L195
- Ruud, M., Loison, J. C., Hickson, K. M., et al. 2015, *MNRAS*, 447, 4004
- Smith, R. S., May, R. A., & Kay, B. D. 2016, *The Journal of Physical Chemistry B*, 120, 1979
- Stevenson, K. P., Kimmel, G. A., Dohnalek, Z., Smith, R. S., & Kay, B. D. 1999, *Science*, 283, 1505
- Takahashi, J., Masuda, K., & Nagaoka, M. 1999, *MNRAS*, 306, 22
- Takahashi, J., & Williams, D. A. 2000, *MNRAS*, 314, 273
- Tielens, A. G. G. M. 2013, *Reviews of Modern Physics*, 85, 1021
- Tielens, A. G. G. M., & Hagen, W. 1982, *A&A*, 114, 245
- Vidali, G. 2013, *Journal of Low Temperature Physics*, 170, 1
- Yuan, C., Cooke, I. R., & Yates, Jr., J. T. 2014, *ApJL*, 791, L21